

Journal of Materials Chemistry A

Materials for energy and sustainability

Accepted Manuscript

This article can be cited before page numbers have been issued, to do this please use: Z. Xiong, W. Wang, Z. Wu, Z. Zhao, Q. Zeng, H. Li, X. Zeng, B. Wu and X. Lai, *J. Mater. Chem. A*, 2025, DOI: 10.1039/D5TA04718H.



This is an Accepted Manuscript, which has been through the Royal Society of Chemistry peer review process and has been accepted for publication.

Accepted Manuscripts are published online shortly after acceptance, before technical editing, formatting and proof reading. Using this free service, authors can make their results available to the community, in citable form, before we publish the edited article. We will replace this Accepted Manuscript with the edited and formatted Advance Article as soon as it is available.

You can find more information about Accepted Manuscripts in the [Information for Authors](#).

Please note that technical editing may introduce minor changes to the text and/or graphics, which may alter content. The journal's standard [Terms & Conditions](#) and the [Ethical guidelines](#) still apply. In no event shall the Royal Society of Chemistry be held responsible for any errors or omissions in this Accepted Manuscript or any consequences arising from the use of any information it contains.

ARTICLE

Received 00th January
20xx,**High-thermopower ionic thermoelectric hydrogel for low-grade heat harvesting and intelligent fire protection**Zizheng Xiong^{a#}, Weiguo Wang^{a,b#}, Zhengzhong Wu^a, Zexi Zhao^a, Qingtao Zeng^a, Hongqiang Li^a, Xingrong Zeng^{a*}, Bowei Wu^c, Xuejun Lai^{a*}

Accepted 00th January 20xx

DOI: 10.1039/x0xx00000x

High thermopower and fire-safety ionic thermoelectric hydrogel is crucial for the development of new energy storage device but full of challenges. Herein, a high-thermopower and flame-retardant ionic hydrogel (HIG) with high ion selectivity was prepared via thermally initiated free-radical polymerization. It was found that the thermoelectric type of HIG transitioned from negative (n-type) to positive (p-type) as the sodium chloride content increased from 0.67 wt% to 1.00 wt%. Afterwards, the ionic thermoelectric pair (p-n junction) with superior thermoelectric performance was constructed. The Seebeck coefficients of n-HIG and p-HIG reached $-1.95 \text{ mV}\cdot\text{K}^{-1}$ and $2.14 \text{ mV}\cdot\text{K}^{-1}$, respectively, while the p-n junction exhibited a much higher Seebeck coefficient of $3.74 \text{ mV}\cdot\text{K}^{-1}$. When being burned, HIG rapidly generated a voltage exceeding 50 mV, and triggered a fire alarm within 4 s, demonstrating excellent thermoelectric efficiency and sensitive early fire-warning capability. Besides, HIG exhibited excellent flame retardancy. Even a propane torch could not ignite HIG within 20 s. The limiting oxygen index (LOI) of wood coated with HIG (Wood@HIG) was higher than 90%, making it rapidly self-extinguishing. Notably, HIG also demonstrated good electrochemical performance and remarkable thermal charging energy storage capabilities, showing good potential for applications in supercapacitors.

1. Introduction

Low-grade waste heat, such as industrial byproducts, biological thermal dissipation, and solar radiation residuals, remains pervasive yet underutilized due to inherent technical challenges.^{1,2} Thermoelectric (TE) materials offer a promising solution for direct thermal-to-electric energy conversion, presenting significant potential to mitigate global energy crises.^{3,4} These materials leverage the Seebeck effect to generate electric potential from thermal gradients, and the phenomenon has garnered more interest in energy harvesting applications.⁵⁻⁷ Traditional electronic thermoelectric (e-TE) material, predominantly composed of inorganic semiconductors and semi-metals, has been thoroughly investigated.^{8,9} However, their practical applications remains constrained by intrinsic characteristics, including low thermopower ($\sim 100\text{-}200 \mu\text{V}\cdot\text{K}^{-1}$), poor flexibility and excessive manufacturing costs.¹⁰

The advent of ionic thermoelectric (i-TE) materials has opened new ways to address the above issues through the Soret effect, achieving exceptional ionic thermopower values at the

$\text{mV}\cdot\text{K}^{-1}$ level.^{11,12} This breakthrough paves a new path for the development of high-thermopower energy storage devices, particularly for low-grade heat recovery technologies.¹³ Nevertheless, there are still numerous challenges that require urgent resolution: phase instability in liquid-state i-TE materials under operational conditions,¹⁴ and the scarcity of negative i-TE material (n-type) to complement prevalent positive thermopower (p-type).^{15,16} In recent years, researchers have focused on the p-n type conversion of quasi-solid i-TE gel (i-TEG) to construct a new type of ionic thermopile (i-thermopile) to further enhance the thermoelectric efficiency, such as 1-ethyl-3-methylimidazolium acetate (Emim:Ac)/H₂O system,¹⁷ 1-ethyl-3-methylimidazole bis(trifluoromethylsulfonyl)imide (Emim:TFSI)¹⁸ and iodide/triiodide (I⁻/I₃⁻) thermogalvanic.^{19,20} These systems combine leakage resistance, mechanical robustness, and fabrication versatility, yet the field remains hindered by the absence of universal mechanisms governing polarity conversion.²¹ Notably, extant studies predominantly concentrate on employing different kind of i-TEGs to construct p-n junction, while achieving selective p-n conversion and superior thermoelectric performance within the same kind of i-TEG material remains a persistent challenge. In addition, the escalating power density and increasingly stringent operational environment of the i-TEG systems necessitate rigorous fire safety standards to ensure sustained performance under the demanding condition. Recent studies include phosphorous-containing ionic liquid (PIL)-based ionogels (PILGs) with rapid fire response (1 s)²² and stretchable PAA-PEO-SDP hydrogels exhibiting high p-type Seebeck coefficients ($24.7 \text{ mV}\cdot\text{K}^{-1}$).²³ However, there were still shortcomings: (i) the low Seebeck coefficient ($1.31 \text{ mV}\cdot\text{K}^{-1}$) of PILGs affected its

^a School of Materials Science and Engineering, Key Lab of Guangdong Province for High Property and Functional Polymer Materials, South China University of Technology, No 381, Wushan Road, Tianhe District, Guangzhou 510640, China.

^b Guangdong Blue Sid&F New Material Co., Ltd, No.43, Electronic Base Factory, Science and Technology West Road, Torch development District, Zhongshan 528437, China.

^c The Affiliated High School of South China Normal University, No.1, Zhongshan Ave. West, Tianhe District, Guangzhou 510630, China.

[#] These authors contributed equally to this work and should be considered co-first authors.

† Electronic Supplementary Information (ESI) available. See DOI: 10.1039/x0xx00000x

thermoelectric conversion efficiency; (ii) the low conductivity ($0.16 \text{ S} \cdot \text{m}^{-1}$) of the PAA-PEO-SDP hydrogels limited its use in integrated devices for energy storage.

Herein, a high-thermopower ionic thermoelectric hydrogel (HIG) for low-grade heat harvesting and intelligent fire protection was prepared. Through precise sodium chloride (NaCl) concentration modulation, we achieved unprecedented p-n-type conversion within a homogeneous material matrix, demonstrating tunable thermopower from -1.95 to $+2.14 \text{ mV} \cdot \text{K}^{-1}$. The p-n junction exhibited a much higher Seebeck coefficient of $3.74 \text{ mV} \cdot \text{K}^{-1}$. The HIG system exhibited sensitive fire-warning capability and excellent flame retardancy, while maintaining superior electrochemical performance and remarkable thermal charging energy storage capabilities, showing good potential for applications in supercapacitors. Our work established a new paradigm in ionic thermoelectric materials by p-n conversion, fire safety, and energy storage in one platform. The NaCl-mediated p-n conversion strategy offers simplicity, scalability, and performance unattainable in existing systems, opening avenues for self-powered fire-protective devices.

2. Experimental section

2.1 Materials

Acrylamide (AAM, 99.0%), carboxymethylcellulose sodium (CMC-Na, 50-200 mPa·s), sodium chloride (NaCl, 99.5%), N,N,N',N'-tetramethylethylenediamine (TEMED, 99.5%), N,N'-methylenebis(acrylamide) (MBA, 97.0%) and ammonium persulphate (APS, 98.0%) were obtained from Aladdin. 2-Acrylamido-2-methyl-1-propanesulfonic acid (AMPSA, 98%) was obtained from Macklin. The above reagents were used directly without further purification.

2.2 Preparation of ionic hydrogel (HIG)

The HIG was fabricated through a one-pot thermally initiated free-radical polymerization. Firstly, a proper amount of AAM, AMPSA, CMC-Na, NaCl, MBAA, APS, and H_2O were placed in a beaker and magnetically stirred at room temperature for 1 h to obtain a transparent and homogeneous mixed solution. Subsequently, a small quantity of APS and TEMED were added and stirred at room temperature for 5 minutes. Subsequently, the mixed solution was transferred into a polytetrafluoroethylene (PTFE) mold, and the heat-induced free radical polymerization was conducted at $65 \text{ }^\circ\text{C}$ in an oven for 1 h, and the n-type and p-type ionic hydrogels (HIG) with high ionic thermoelectric properties were prepared. The corresponding formulation is presented in **Tab. S1**.

2.3 Preparation of HIG thermoelectric supercapacitor and p-n junction

The p-HIG and n-HIG were cut into rectangular specimens ($10 \text{ mm} \times 10 \text{ mm} \times 1.5 \text{ mm}$), then laminated with carbon cloth electrodes on the upper and lower surfaces of the hydrogels. The electrode was composed of activated carbon, conductive carbon black, and polyvinylidene fluoride, and their mass ratio was 8:1:1.

Subsequently, two copper foil tapes ($30 \text{ mm} \times 10 \text{ mm} \times 0.1 \text{ mm}$) were affixed to the two ends surfaces of the electrodes to connect the circuit, and the contact area between the copper foil and the carbon cloth electrode was $10 \text{ mm} \times 10 \text{ mm}$. For the convenience of experimental testing, two layers of silicone rubber (SiR) pads ($10 \text{ mm} \times 10 \text{ mm} \times 2 \text{ mm}$) were placed at up and down surfaces of the supercapacitor prior to its sealing with polyimide tape, and then the HIG thermoelectric supercapacitor (HIG SC) was assembled, as shown in **Fig. S1a**.

The schematic diagram of p-n junction thermoelectric pair (p-n junction) is shown in **Fig. S1b**. The p-HIG/n-HIG ($30 \text{ mm} \times 10 \text{ mm} \times 1.5 \text{ mm}$) were fabricated by connecting the two ends in series with copper foil tape. The p-n junction was set up in a "II" shape to ensure the cold end and the hot end of p-HIG/n-HIG were consistent.

2.4 Preparation of ionic Wood@HIG

The prepared HIG (with a thickness of approximately 0.5 mm) was cut into the desired size and then firmly adhered to the surface of the commercial larch wood strips by taking advantage of its excellent self-adhesive performance, thereby obtaining the wood strip sample (Wood@HIG) with a fire warning function.

3. Results and discussion

3.1 The design strategy and characterization of HIG

The design strategy and functions of HIG is illustrated in **Fig. 1**. HIG was fabricated via a one-pot thermally initiated free-radical polymerization method, and its n-type to p-type transition was achieved by introducing NaCl. The p-n junction was constructed by combining the n-HIG and p-HIG with copper foils. **Fig. S3a** shows the Fourier transform infrared spectroscopy (FTIR) of AAM, AMPSA and poly (AAM/AMPSA). The characteristic absorption peaks of AAM included: the C=C stretching vibration at 1612 cm^{-1} , the asymmetric and symmetric N-H stretching vibrations of the primary amine group ($-\text{NH}_2$) at 3351 cm^{-1} and 3187 cm^{-1} , respectively, and C=O stretching vibration at 1673 cm^{-1} .²⁴ For AMPSA, the characteristic vibration peaks were observed at 1083 cm^{-1} and 1243 cm^{-1} (attributed to $-\text{SO}_3^-$ stretching vibrations), while the absorption peaks at 1666 cm^{-1} and 1612 cm^{-1} corresponded to the stretching vibrations of C=O and C=C.²⁵ The poly (AAM/AMPSA) copolymer revealed the disappearance of the C=C characteristic peaks from both AAM and AMPSA monomers, confirming the completion of the copolymerization. Notably, the C=O stretching vibration peaks near 1668 cm^{-1} remained observable in the copolymer. The N-H stretching vibration peak of the copolymer exhibited a red shift to 3380 cm^{-1} , presumably caused by the spatial constraints of the polymer backbone and the reduced density of $-\text{NH}_2$ groups.²⁶ Similarly, the $-\text{SO}_3^-$ vibration peaks also red-shifted to 1041 cm^{-1} and 1197 cm^{-1} , which could be ascribed to the intermolecular interactions between the $-\text{NH}_2$ and $-\text{SO}_3^-$ groups.²⁷ The above results basically confirmed the successful synthesis of poly (AAM/AMPSA) copolymer.

Fig. S3b shows the FTIR spectra of CMC-Na and p-HIG/n-HIG gels. The addition of CMC-Na did not obviously change the positions of the functional groups in the poly (AAM/AMPSA)

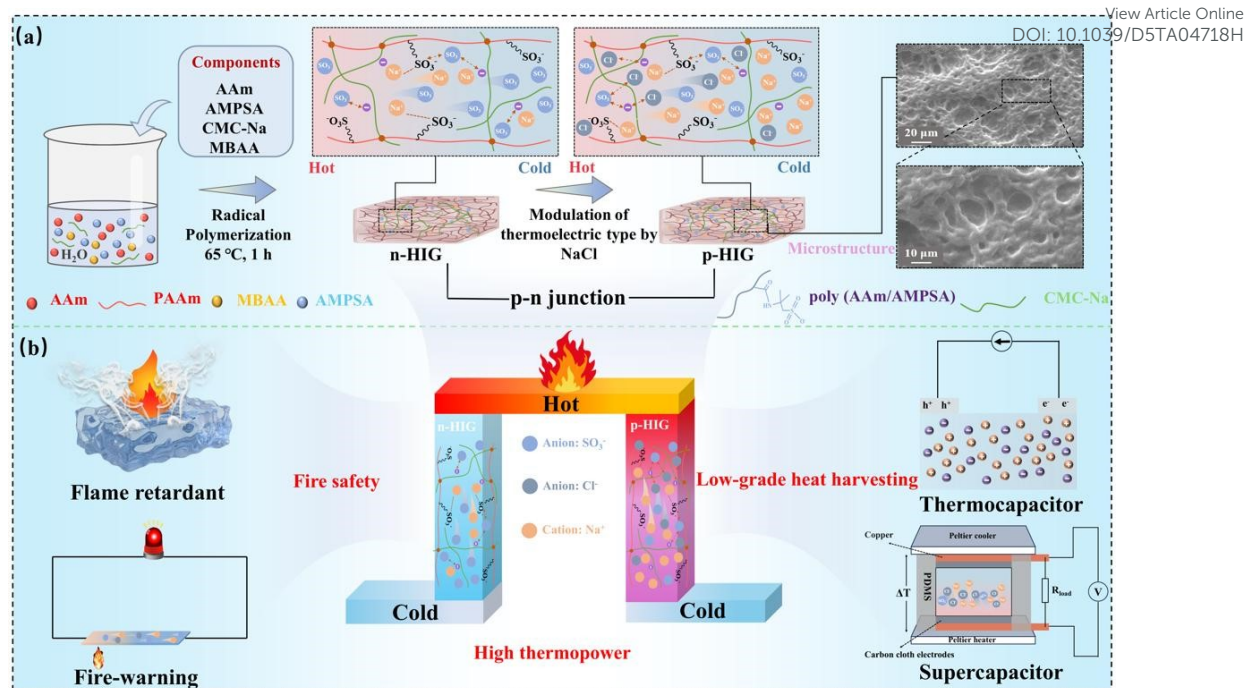


Fig. 1 (a) Schematic diagram of the preparation of Hig; (b) Construction of the p-n junction and the function of the Hig.

system. This phenomenon may be attributed to two factors: the partial overlap between the absorption bands of polar groups ($-\text{COO}^-$ and $-\text{OH}$) in CMC-Na and those of $-\text{SO}_3^-$ and $-\text{NH}_2$ in the copolymer; and the absence of strong chemical interactions among the three components.^{24,28} Furthermore, the homogeneous distribution of micro-nanochannels in the hydrogel interpenetrating network for Hig is demonstrated in scanning

electron microscope (SEM) images of Fig. 1a. The findings confirmed that the incorporation of CMC-Na did not significantly alter the chemical structural features of poly (AAm/AMPSA) hydrogels, and also revealed that the uniformly distributed micro- and nanochannel structures within them were the key morphological basis to support efficient anion/cation synergistic transport.

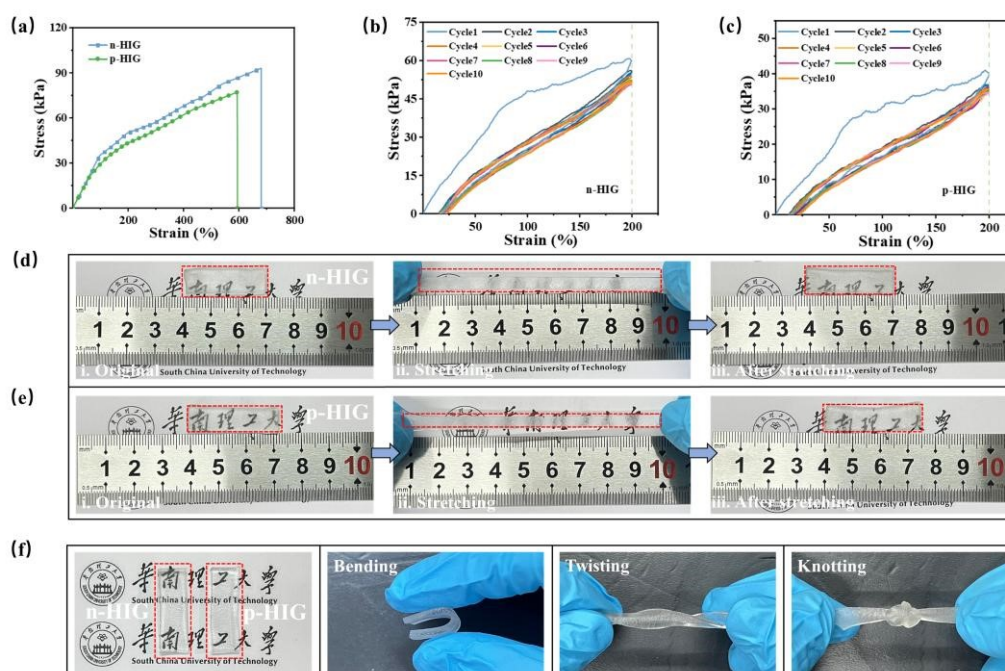


Fig. 2 (a) Tensile stress-strain curves of n-HIG/p-HIG; Tensile stress-strain curves of (b) n-HIG and (c) p-HIG with 10 cycles; video screenshots of tensile recovery of (d) n-HIG and (e) p-HIG; (f) Digital photographs and flexibility of Hig.

3.2 Mechanical properties of HIG

Mechanical properties of the hydrogels are summarized in Fig. 2. From Fig. 2a, the tensile strength and elongation at break of p-HIG decreased with the NaCl incorporation, which was attributed to the weakening of intermolecular interactions between the polymer chains by the addition of inorganic salt.²⁹ The tensile strength and elongation at break of p-HIG were 79.8 kPa and 587%, whereas the tensile strength and elongation at break of n-HIG without NaCl were 92.6 kPa and 609%, which were 1.16 and 1.02 times higher than those of p-HIG. Fig. 2b, c display the stress-strain curves of n-HIG and p-HIG for 10 stress loading/unloading cycles at 50% strain. The good overlap of stress-strain curves across 10 consecutive loading-unloading cycles at 50% strain confirmed minimal energy dissipation and structural integrity retention in both systems. HIG also possessed excellent flexibility and tensile resilience as illustrated in Fig. 2d-f. It could be observed that the hydrogel retained structural integrity after severe deformation (180° bending, twisting, and knotting) and fully recovered its original shape even after undergoing >200% tensile strain. Additionally, we investigated the variation in mechanical properties of HIG with NaCl content, as presented in Fig. S4. The findings indicated that although the addition of NaCl weakened the intermolecular forces, leading to a slight decline in the tensile performance of the p-HIG component, this hydrogel system still exhibited low energy dissipation, excellent flexibility, structural integrity, and shape recovery capability.

3.3 Thermoelectric properties of HIG

The ionic thermoelectric conversion performance of p-HIG, n-HIG, and their constructed ionic thermoelectric pair (p-n

junction) is shown in Fig. 3. All three configurations displayed real-time response, repeatability, and linear thermoelectric behavior. Quantitative analysis revealed that when subjected to temperature gradients increasing from 5 K to 20 K, the output voltages increased from -9.2 mV to -38.6 mV for n-HIG, 10.8 mV to 43.4 mV for p-HIG, and 14.8 mV to 73.7 mV for the p-n junction. Furthermore, n-HIG, p-HIG, and the p-n junction exhibited rapid temperature response (response time < 1 s) and reproducible thermoelectric performance, highlighting their potential for applications such as temperature sensing and early fire warning systems. Linear regression analysis of the voltage-temperature revealed a strong linear correlation ($R^2 = 0.999$ for n-HIG, 0.998 for p-HIG) between the thermal voltage and applied ΔT for all configurations. The slope of the fitting line corresponded to the ionic Seebeck coefficient (S_i), which directly determined the thermal voltage generated per unit temperature gradient. The measured S_i values were $-1.95 \text{ mV}\cdot\text{K}^{-1}$, $2.14 \text{ mV}\cdot\text{K}^{-1}$, and $3.74 \text{ mV}\cdot\text{K}^{-1}$ for n-HIG, p-HIG, and the p-n junction. These results indicated that n-HIG and p-HIG possessed comparable yet opposite thermoelectric polarities, while the p-n junction achieved a synergistic enhancement in ionic thermoelectric efficiency (91.4% of the combined thermoelectric contributions from n-HIG and p-HIG). Notably, the p-n junction exhibited enhanced thermoelectric conversion efficiency compared to individual components. This enhancement arose from the structural compatibility and nearly equivalent thermoelectric capacities of the individual components, enabling the p-n junction to effectively amplify the cumulative thermal voltage through their series configuration.^{12,30} While the p-n junction achieved 91.4% synergistic efficiency, two key factors limit further

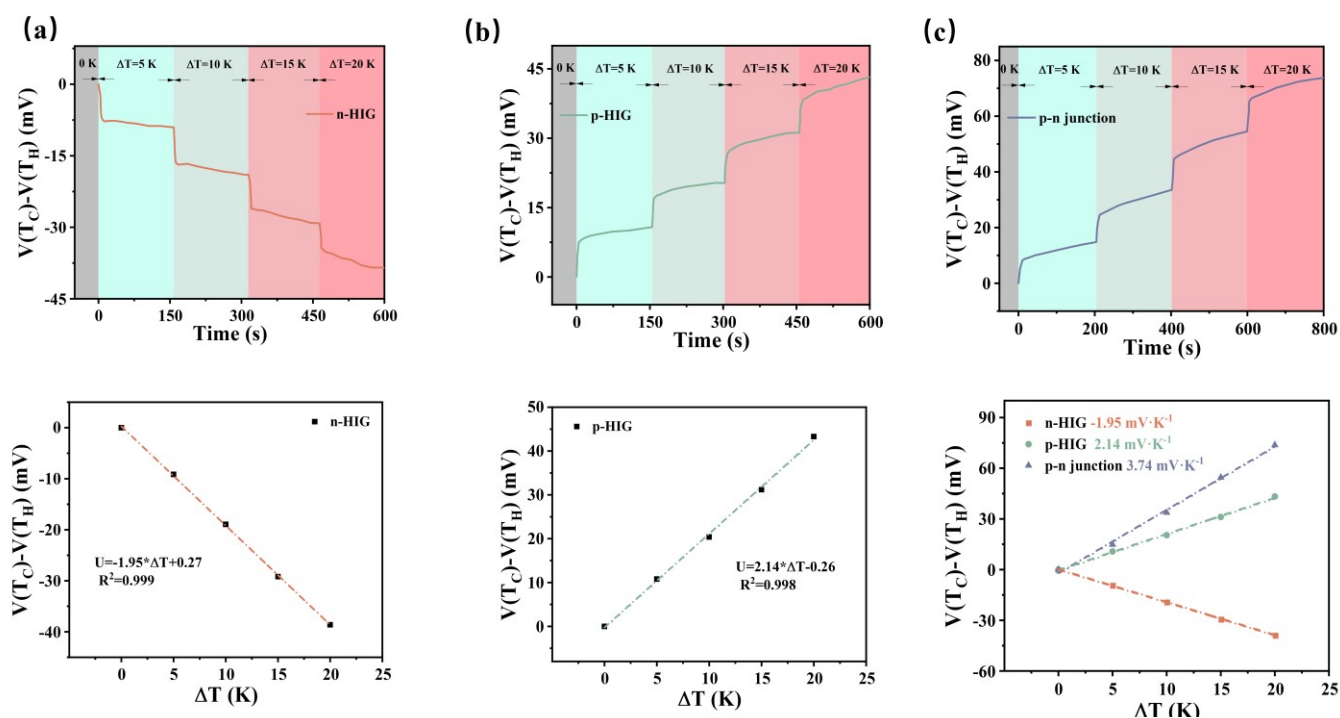


Fig. 3 Voltage response curves and fitted linear curves between thermoelectric voltage and temperature difference of (a) n-HIG and (b) p-HIG; (c) Voltage response curves and fitted linear curves between thermoelectric voltage and temperature difference of p-n junction.

enhancement: (i) Interfacial contact resistance:³¹ the copper/HIG interfaces introduced additional electrical resistance, dissipating thermal energy as Joule heat rather than convertible potential; (ii) Thermal contact losses: the copper foils exhibited high thermal conductivity ($\sim 390\text{--}400\text{ W}\cdot\text{m}^{-1}\cdot\text{K}^{-1}$),³² which caused a portion of the heat to be absorbed by the copper foil, thereby reducing the effective temperature gradient across the p-n junction. The

thermal loss directly affected the performance of the thermoelectric device by lowering the available thermal energy for conversion.

To investigate the ionic thermoelectric conversion mechanism of n-HIG and p-HIG, SEM-EDS was employed to characterize the elemental distribution across HIG cross-sections. The specific operation is shown in Fig. 4a, n-HIG and

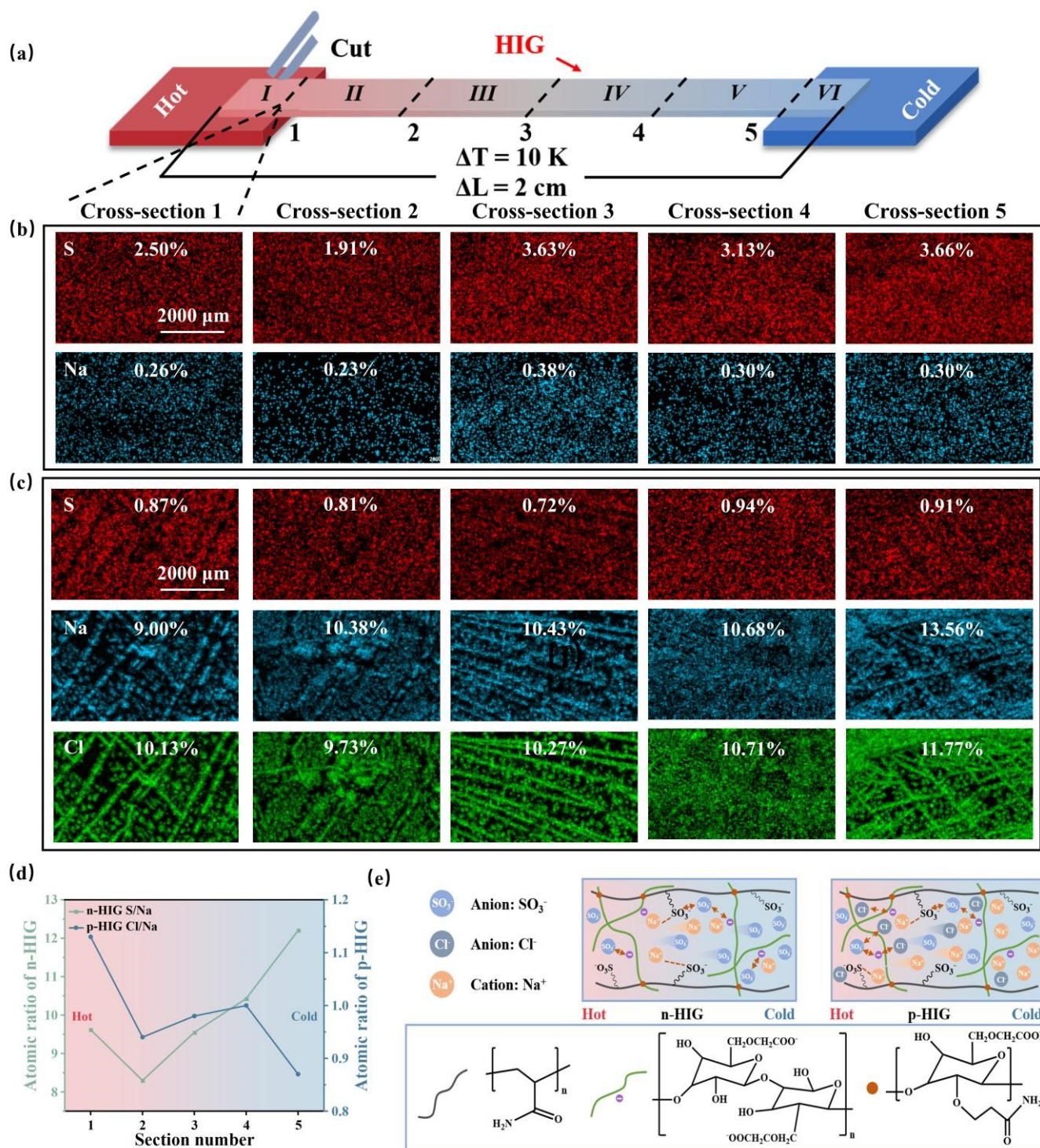


Fig. 4 Schematic diagram of the segmental sampling operation of HIG; Distribution of the corresponding elements under different cross-sections of (b) n-HIG and (c) p-HIG; (d) Corresponding stoichiometric ratios; (e) Schematic illustration of ionic thermal diffusion mechanism.

p-HIG were maintained under 10 K for 1 h, and then quickly cut into six interval segments, followed by rapid freezing with liquid nitrogen and cold-drying for 24 h. EDS mapping quantified sulfur (S), chlorine (Cl), and sodium (Na) distributions across five regions spanning the hot-to-cold axis. As shown in **Fig. 4b, c and Fig. S5**, the concentrations of S, Cl, and Na exhibited a gradual increase from the hot end to the cold end, reaching their highest levels at the cold end. This observation indicated that free anions and cations migrated from the hot end to the cold end under thermal driving forces. In n-HIG, S and Na contents at the hot end were measured as 2.50% and 0.26%, while those at the cold end increased to 3.66% and 0.30%. The S/Na ratio (**Fig. 4d**) at the cold end (12.20) significantly exceeded that at the hot end (9.62), demonstrating that the quantity of SO_3^- groups in the n-HIG system not only substantially surpassed that of Na^+ ions but also exhibited greater thermal migration capability. Consequently, the accumulation of SO_3^- at the cold end markedly exceeded that of Na^+ . Conversely, p-HIG exhibited Cl and Na enrichment at the cold end (11.77% and 13.56%) versus hot-end concentrations (10.13% and 9.00%), with negligible S content (0.87%). Notably, the cold-end Na:Cl ratio (0.87) decreased relative to the hot end (1.13). This phenomenon arose from two factors:^{33,34} (i) The smaller ionic radius of Na^+ compared to Cl^- enabled faster cation migration, leading to Na^+ accumulation and consequent positive charge accumulation at the cold end; (ii) The dual-crosslinked anionic network formed by dissociated CMC^- and poly (AAm/AMPSA) copolymer chains significantly hindered the migration of Cl^- and SO_3^- anions due to electrostatic repulsion. In contrast, Na^+ cations exhibited enhanced thermal diffusion capability under temperature gradients. These combined effects resulted in cation-selective transport behaviour within the HIG system. The ion thermoelectric conversion mechanisms of n-HIG and p-HIG are schematically illustrated in **Fig. 4e**.³⁵ In the absence of a temperature gradient, anions and cations remained uniformly distributed within the hydrogel matrix, maintaining electrical neutrality. After applying a temperature gradient, thermally driven ion diffusion induced directional migration of Cl^- , SO_3^- , and Na^+ toward the cold end. In n-HIG systems, the substantially higher population of SO_3^- groups (compared to Na^+) led to predominant accumulation of negative charges at the cold end, generating a net negative potential. Conversely, in p-HIG systems, the faster migration rate and greater mobility of Na^+ cations (relative to anions) resulted in excessive positive charge accumulation at the cold end. This asymmetric charge distribution elevated the local potential, thereby demonstrating p-type ionic thermoelectric behaviour. In order to clarify the effect of AMPSA on the thermoelectric properties of HIG, formulations with varying AMPSA content were systematically investigated (**Tab. S2**). As shown in **Fig. S6**, all HIG samples exhibited n-type ionic thermoelectric behavior. The ionic Seebeck coefficient displayed a non-monotonic dependence on the AMPSA concentration, reaching an optimal value of $-1.95 \text{ mV}\cdot\text{K}^{-1}$ before diminishing with further increases in AMPSA content. This was mainly attributed to the interplay between the mobile sulfonate groups (SO_3^-) and the overall charge distribution within the HIG structure. At low AMPSA concentration, the increased density of SO_3^- groups enhanced charge

accumulation at the cold end under a thermal gradient, thereby amplifying the negative thermovoltage generation and leading to a higher Seebeck coefficient. However, as the AMPSA content increased beyond the optimal level, the presence of electronegative gel molecular chains and the electrostatic repulsion between free SO_3^- ions begin to dominate. This resulted in a gradual reduction of negative charge accumulation at the cold end, ultimately causing the ionic Seebeck coefficient to diminish. To elucidate the role of NaCl in the p-n transition, we conducted a series of experiments with hydrogel formulations containing varying trace amounts of NaCl (0, 0.067, 0.33, 0.67, 1.00, and 1.33 wt%). We measured the Seebeck coefficients of these hydrogels and compared them with those of all hydrogels listed in **Tab. S1**. The results are presented in **Fig. S7 and S8**. The results indicated that below 0.67 wt% NaCl, the hydrogel (n-HIG) was dominated by sulfonate groups ($-\text{SO}_3^-$) from AMPSA, SO_3^- accumulated at the cold end by virtue of its quantity, so that a net negative thermal voltage was generated (n-type). When the sodium chloride (NaCl) content increased, the number of Na^+ ions became sufficiently high, their faster migration rate and greater mobility led to excessive accumulation of positive charge at the cold end. Simultaneously, the dual-crosslinked anionic network formed by dissociated CMC^- and poly (AAm/AMPSA) copolymer chains significantly hindered the migration of Cl^- and SO_3^- anions due to electrostatic repulsion. Consequently, with increasing NaCl content, the magnitude of the ionic Seebeck coefficient of HIG also increased, ultimately resulting in p-type thermoelectric behavior (NaCl >1.00 wt%).

3.4 Fire warning performance

Benefiting from exceptional ionic thermoelectric properties, HIG demonstrates significant application potential in self-powered smart fire-protection systems. As shown in the schematic of fire-warning test (**Fig. 5a**), thermal gradients induced directional migration of ions in HIG, generating a thermovoltage through charge accumulation at the cold end. When the thermovoltage exceeded a predefined threshold (50 mV), the alarm system was autonomously triggered. Both n-HIG and p-HIG generated voltage signals without external power input, enabling fully self-powered fire warning responses. The voltage response profiles (**Fig. 5b, c**) reveal that HIG maintained a low baseline voltage at ambient temperature. Under localized flame exposure, a rapid temperature gradient induced swift ion migration, causing an abrupt voltage surge. Specifically, n-HIG activated the alarm within 4.3 s, while p-HIG achieved a thermoelectric potential exceeding 50 mV in merely 3.5 s, highlighting ultrafast fire-detection capabilities. Markedly, the thermovoltage spontaneously reverted to baseline after heat removal, confirming HIG's reversible fire-warning capability. Repeatability tests further verified stable performance over three consecutive ignition cycles. As shown in **Fig. 5d**, p-HIG consistently achieved shorter response times during three consecutive ignition tests. This enhancement could be attributed to the incorporation of NaCl, which introduced a high concentration of smaller-sized and faster-migrating Na^+ ions. It could significantly improve fire-warning efficiency.

Fig. 6a, b show the video screenshot of the fire warning test of HIG, confirming HIG's repeatable fire-warning capability. When exposed to flame, n-HIG generated a thermovoltage of

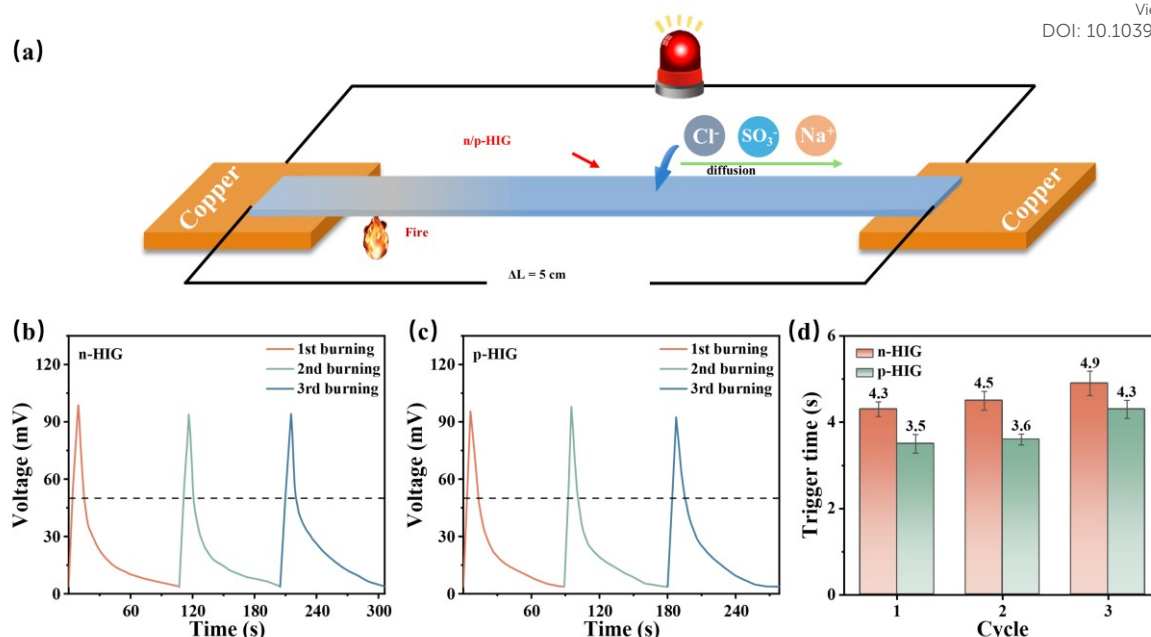


Fig. 5 Fire-warning functionality evaluation of HIG: (a) Schematic of testing principle; Fire-response voltage curves of (b) n-HIG and (c) p-HIG; (d) The trigger time of n-HIG and p-HIG.

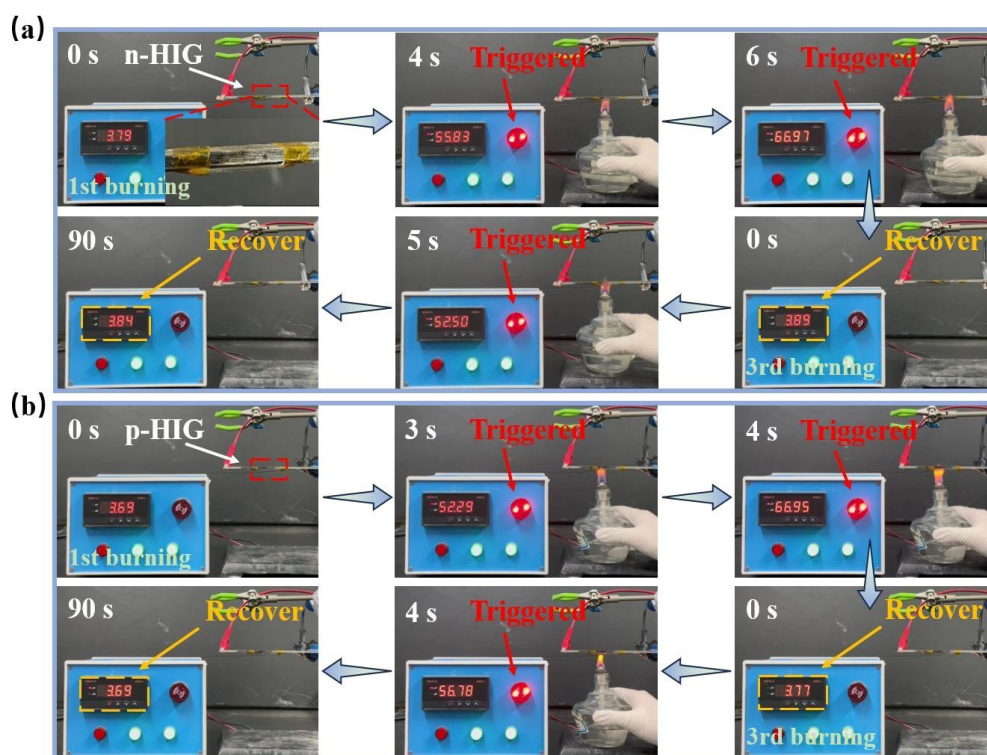


Fig. 6 Fire-warning testing of HIG: Video screenshots of (a) n-HIG and (b) p-HIG during the first and third fire-warning test.

55.8 mV within 4 s, activating the alarm system. After the flame removal, the thermal potential rapidly decayed to its baseline value (3.8 mV). In cyclic ignition tests, n-HIG demonstrated sustained responsiveness, consistently producing thermovoltage exceeding 50 mV within ~5 s. Similarly, p-HIG achieved superior repeatability, enabling multiple warnings with shorter activation times during repeated thermal stimuli. Following three consecutive fire-warning cycles, both n-HIG and p-HIG

maintained reproducible performance. The above results confirmed the fast response (<5 s), high output thermal voltage (>50 mV), excellent cyclic stability, and highly reproducible fire warning capability of n-HIG and p-HIG for fire warning applications.

3.5 Flame retardancy

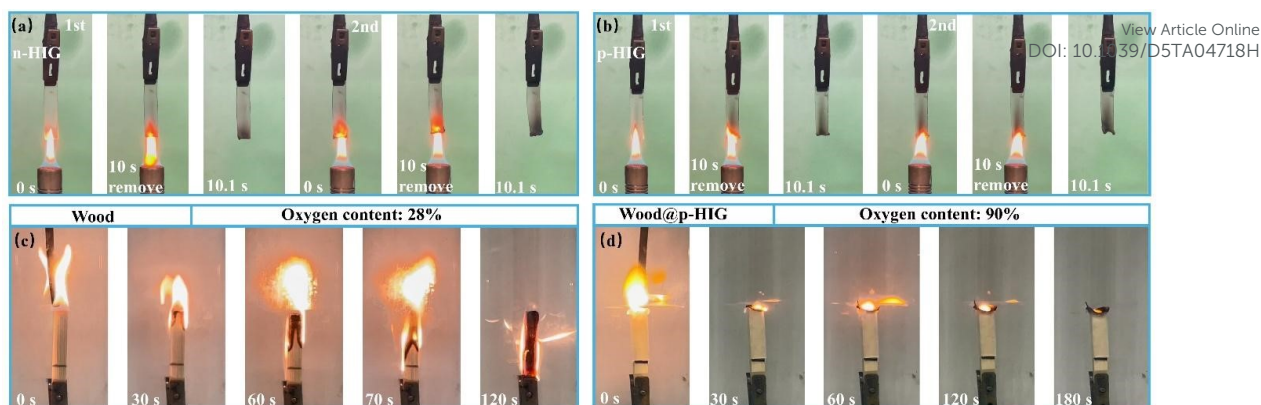


Fig. 7 Video screenshots of the vertical combustion of (a) n-HIG and (b) p-HIG; Video screenshots of (c) Wood burning at the atmosphere with 28% oxygen and (d) Wood@p-HIG burning at the atmosphere with 90% oxygen.

Fig. S9 and **Fig. 7a, b** present the results of the flame retardancy tests of Wood, Wood@n-HIG, Wood@p-HIG, n-HIG and p-HIG. As can be seen from **Fig. 7a, b**, both n-HIG and p-HIG exhibited exceptional flame retardancy: After two consecutive 10s exposures to a Bunsen burner flame, only localized charring occurred at the bottom edges, with no flame propagation, accompanied by self-extinguishing behavior after the flame removal. Compared with HIG, the flame of Wood spread rapidly after ignition and was almost completely burnt after 130 s (**Fig. S9a**), with a limiting oxygen index (LOI) far

below 28% (**Fig. 7c**). Under HIG protection, both Wood@n-HIG and Wood@p-HIG remained non-ignitable after two flames burnt, sustaining only localized charring at the base while protecting the wood substrate (**Fig. S9b, c**). Visibly, Wood@p-HIG retained superior flame resistance even under extreme conditions (oxygen concentration of 90%) (**Fig. 7d**). Microscale combustion calorimetry (MCC) further quantified the thermal release properties of polyacrylamide gel (PAAm), n-HIG, and p-HIG (**Tab. S3**). Compared to PAAm, n-HIG and p-HIG exhibited significant reductions in heat release capacity, peak

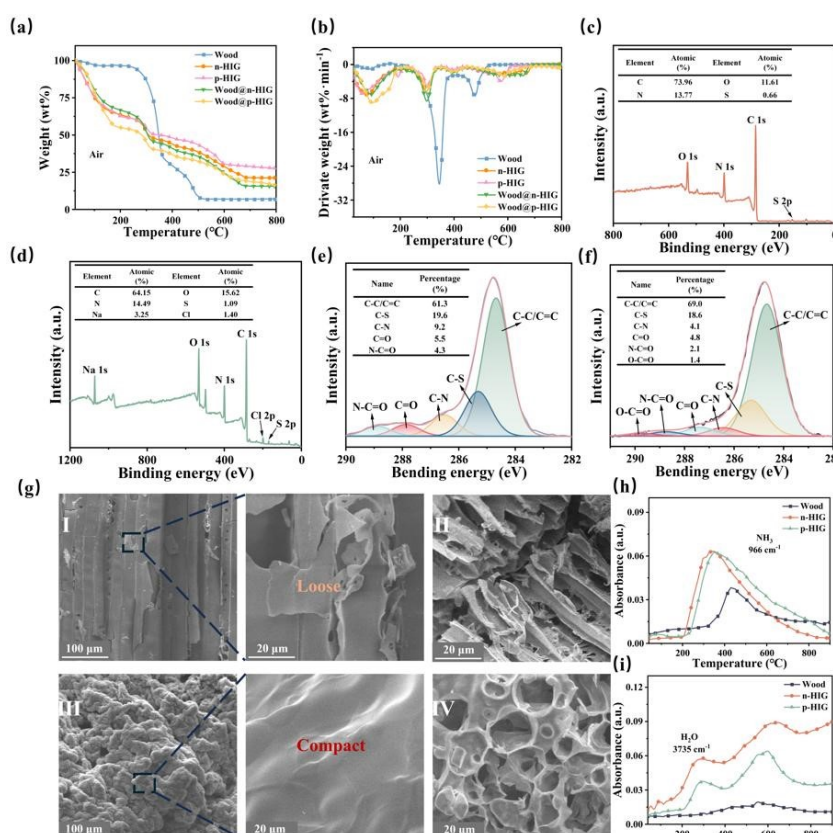


Fig. 8 (a) TG and (b) DTG curves for Wood, n-HIG, p-HIG, Wood@n-HIG and Wood@p-HIG under air atmosphere; XPS spectra of char layer of (c) n-HIG and (d) p-HIG after combustion; C 1s XPS spectra of p-HIG (e) before and (f) after combustion; (g) SEM images of (I) surface and (II) cross-section char layer of Wood after combustion; (III) surface and (IV) cross-section char layer of Wood@p-HIG after combustion; Absorbance of pyrolysis products (h) H₂O; (i) NH₃ of Wood, n-HIG and p-HIG as a function of time.

heat release rate, and total heat release. Concurrently, their PHRR temperatures increased to 371°C and 376°C, indicating enhanced fire safety.

3.6 Flame retardant mechanism of HIG

Fig. 8a, b show the TG and DTG curves of Wood, n-HIG, p-HIG, Wood@n-HIG and Wood@p-HIG under air atmosphere. Comparative analysis revealed that HIG coating significantly enhanced the thermal stability of wood. The residual mass of Wood at 800 °C was 7.2 wt%, exhibiting a maximum mass loss rate of 28.2 wt%·min⁻¹ at 345.3°C. In contrast, HIG-coated wood composites (Wood@n-HIG and Wood@p-HIG) demonstrated markedly improved thermal resistance, retaining approximately 16.5 wt% residual mass at 800°C and achieving a reduced peak mass loss rate of 8.6 wt%·min⁻¹ at 297.0°C. Critically, no detectable mass loss occurred near 345.3°C for the HIG-coated systems, indicating a marked enhancement in the thermal stability of wood.

The microstructural evolution of char layers formed during vertical combustion of Wood and Wood@p-HIG was investigated via SEM, as shown in **Fig. 8g**. Wood developed a loose, porous char layer after combustion (**Fig. 8g I and II**), facilitating oxygen infiltration and heat transfer to accelerate internal thermal degradation and flammable volatiles release. In contrast, Wood@p-HIG formed a continuous dense char layer with uniformly distributed micropores (**Fig. 8g III and IV**), acting as an effective thermal/flammable gas barrier to suppress combustion propagation.^{36,37}

The XPS analysis for the char layers of n-HIG and p-HIG are displayed in **Fig. 8c-f**. The retention of flame-retardant elements in char layer for p-HIG (14.49% N, 1.40%Cl, 1.09% S) (**Fig. 8d**). Comparative C 1s spectral analysis (**Fig. 8e-f**) demonstrated that the C-C/C=C content of the char layer increased from 61.3% to 69.0%, while the C-S and C-N contents decreased from 19.6% and 9.2% to 18.6% and 4.1%, alongside

newly formed -O-C=O groups after combustion. These chemical transformations indicated that more thermally stable conjugated structures were formed in the p-HIG char layer and flame-retardant substances such as NH₃ can exert a flame retardant effect in the gas phase.³⁸

To further elucidate the flame retardant mechanism of HIG, thermogravimetric-Fourier transform infrared spectroscopy (TG-FTIR) was employed to analyze thermal degradation volatiles from Wood, n-HIG, and p-HIG (**Fig. 9**). The pyrolysis products of Wood included more flammable gases such as alkanes, CO and carbonyl compounds, which fuel combustion reactions.³⁹ In contrast, the signal intensity of H₂O generated by n-HIG and p-HIG during combustion was about 6-8 times that of Wood, and the signal intensity of flame-retardant gases, such as NH₃, was close to 2-3 times (**Fig. 8h, i**), while the signal intensity of flammable gases generated was much lower. During initial pyrolysis, HIG released substantial water vapor, effectively suppressing substrate temperature rise via latent heat of vaporization.^{40,41} As the combustion continued, the acylamino group in n-HIG and p-HIG started to decompose, releasing NH₃ at about 280 °C, diluting the combustible gases and oxygen,^{42,43} reducing the combustion reaction in the gas phase.

In summary, HIG demonstrated exceptional flame retardancy through synergistic effects involving both gas-phase dilution and condensed-phase barrier formation (mechanism schematic as shown in **Fig. 10**). During initial combustion, HIG rapidly released water vapor to dilute flammable gases and suppress temperature rise via endothermic vaporization. When the temperature increased, decomposition of -NH₂ groups in HIG generated non-flammable NH₃, further reducing oxygen availability and combustible gas concentrations to retard flame propagation. In addition, HIG's intrinsic porous network structure and gas-release behaviour promoted the formation of abundant microcavities during pyrolysis,

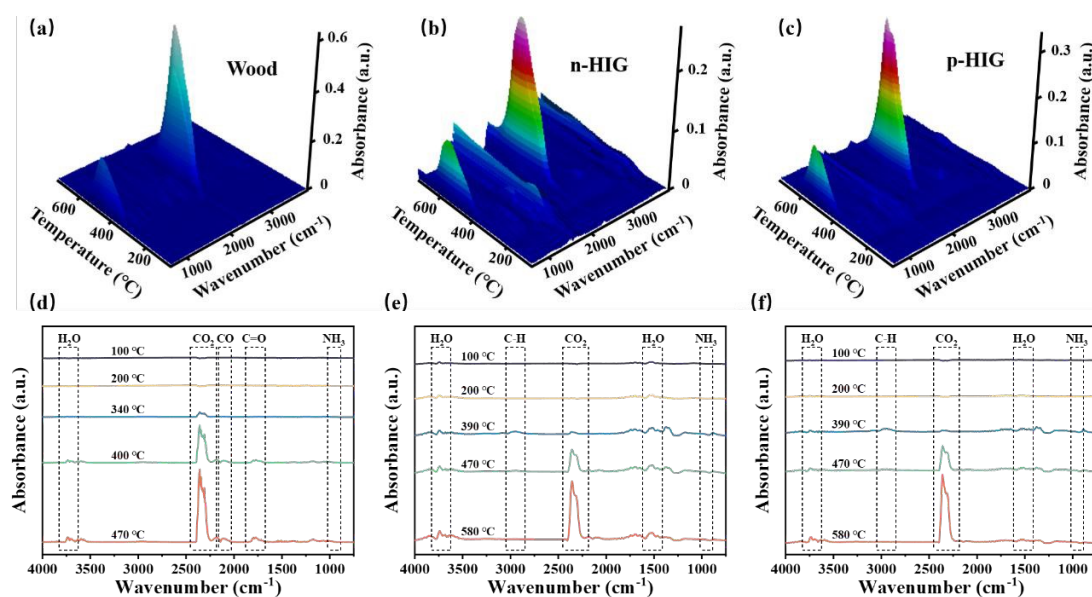


Fig.9 3D TG-FTIR spectra of pyrolysis products and the corresponding FTIR spectra of (a, d) Wood; (b, e) n-HIG and (c, f) p-HIG at different temperatures under air atmosphere.

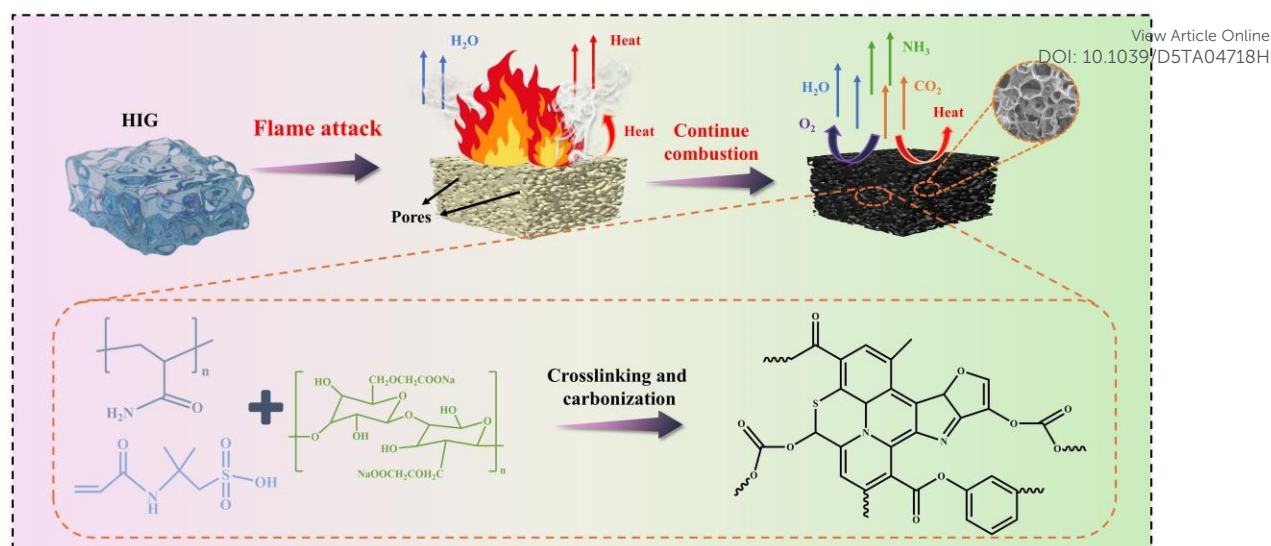


Fig. 10 Schematic diagram of the flame-retardant mechanism of HIG.

ultimately yielding a uniform, dense expanded char layer. This hierarchical char barrier effectively blocked heat/oxygen transfer while inhibiting thermal degradation of the gel matrix or protected substrates. This synergistic effect realized a flame retardant effect in the gas phase - condensed phase and significantly improved the fire safety of flammable materials as a fire protection layer.

3.7 Thermal capacitance properties

HIG demonstrated exceptional ionic thermoelectric properties, positioning it as a multifunctional material for temperature sensing, fire warning systems, and low-grade heat harvesting. As illustrated in Fig. 11a, ionic thermocapacitors were constructed by assembling HIG with copper foil (Cu) electrodes, enabling thermoelectric conversion and energy storage via a four-stage capacitive cycle: Thermal gradient-driven charging was the first stage. Under a temperature gradient,

directional ion migration occurred within the thermocapacitor. Faster Na^+ migration relative to Cl^- in p-HIG induced positive charge accumulation at the cold end, generating a forward thermovoltage. In the second stage, connecting the external circuit triggered electron transfer via the electric double-layer (EDL) effect between HIG and Cu, achieving charge equilibration and power output, and this stage was named the energy output. The third stage was about temperature gradient removal, removing the thermal gradient while disconnecting the circuit allowed ionic redistribution, creating a reverse voltage. The final stage was reverse discharging, reconnecting the load allowed electrons to migrate again, thereby delivering additional electrical energy to the external circuit. Fig. 11b-d confirmed that n-HIG, p-HIG, and p-n junction thermocapacitors followed identical operational logic: thermovoltage generation during charging, electron migration across electrodes, voltage decay

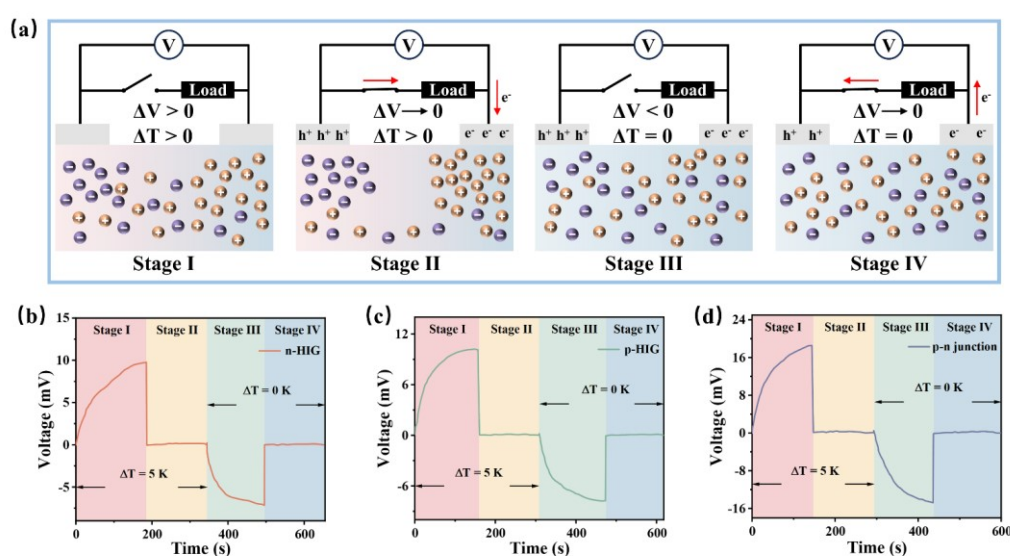


Fig. 11 (a) Schematic diagram for operation principle of HIG thermoelectric capacitor; Four stage voltage curve of (b) n-HIG; (c) p-HIG and (d) p-n junction thermoelectric capacitor during heat harvesting.

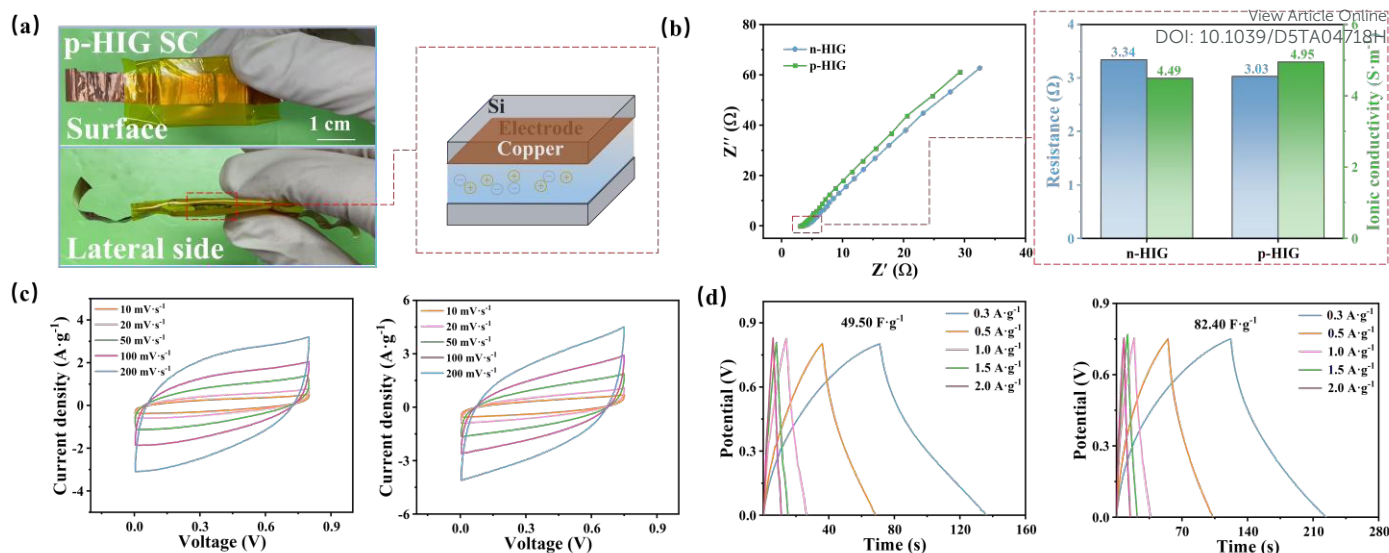


Fig. 12 (a) Digital photograph and schematic of HIG SC; (b) EIS curves, electrochemical impedance values and ionic conductivity of n-HIG and p-HIG; (c) CV curves and (d) GCD curves of n-HIG SC and p-HIG SC.

during discharging, and reverse charging for energy delivery. Under a 5 K temperature gradient, all thermocapacitors exhibited slightly lower open-circuit voltages than their standalone HIG counterparts, exhibiting excellent conversion capabilities. The p-n junction thermocapacitor achieved a thermovoltage of 18.6 mV (5 K ΔT), accounting for 92% of the summed outputs from n-HIG and p-HIG units. This aligns with the theoretical relationship $|S_{p-n}| \approx 0.914 \times (|S_n| + |S_p|)$, demonstrating rational energy conversion synergy.

Furthermore, as shown in Fig. S10, the open-circuit voltage and maximum output power of the n-HIG, p-HIG, and p-n junction thermocapacitors increased significantly with rising temperature gradients, indicating that a larger temperature difference enhanced the conversion of thermal energy into electrical energy. At a temperature gradient of 20 K, the maximum output power of the p-HIG thermocapacitor reached 109.0 nW, approximately 2.7 times that of the n-HIG thermocapacitor. This enhancement originated from two synergistic advantages of p-HIG: higher thermovoltage generation (2.14 mV·K⁻¹) and superior mobility of mobile Na⁺ ions compared to SO₃⁻ in n-HIG, enabling stronger current output. Additionally, the p-n junction thermocapacitor achieved a thermal a thermovoltage of -66.3 mV and peak power of 157.4 nW, corresponding to over 90% of the summed outputs from individual n-HIG and p-HIG units. The rationally designed p-n junction architecture synergistically combined the cation-dominant transport of p-HIG with the anion-enhanced thermopower of n-HIG, collectively elevating the thermoelectric conversion efficiency of hydrogel-based systems.

3.8 Electrochemical and thermal charging properties of HIG SC

The electrochemical impedance spectroscopy (EIS) spectra and ionic conductivity (σ_i) of HIG are presented in Fig. 12b. p-HIG exhibited superior ionic conductivity (4.95 S·m⁻¹) compared to n-HIG, primarily attributed to its higher population of mobile ions. Both n-HIG and p-HIG demonstrated sufficiently high σ_i valued (>3 S·m⁻¹), making them suitable for flexible

sensing (Fig. S11) and functioning as quasi-solid-state supercapacitors (denoted as n-HIG SC and p-HIG SC), as shown in Fig. 12a. Cyclic voltammetry (CV) curves of n-HIG SC and p-HIG SC were evaluated at scan rates of 10–200 mV·s⁻¹ within a 0–0.75 V window (Fig. 12c). Both devices exhibited quasi-rectangular CV curves at low scan rates (10–20 mV·s⁻¹), retaining centrosymmetric shapes without distortion at elevated rates, indicative of ideal electric double-layer capacitive behavior and high-rate capability. Galvanostatic charge-discharge (GCD) curves further confirmed capacitive characteristics, displaying highly symmetrical triangular profiles. At 0.3 A·g⁻¹, n-HIG SC and p-HIG SC achieved specific capacitances of 49.5 F·g⁻¹ and 82.4 F·g⁻¹, respectively (Fig. 12d). The superior performance of p-HIG SC was attributed to NaCl-induced elevation in free ion concentration, abundant free ions penetrated and transferred to facilitate efficient EDL formation at electrode-electrolyte interfaces. Thus, the number of ions involved in charge exchange during capacitance formation increased, allowing the electrode surface to hold and convert more charge.⁴⁴

Leveraging the exceptional ionic thermoelectric properties of HIG, HIG SC operated as a multifunctional device, combining quasi-solid-state energy storage with ionic thermoelectric conversion. Given its superior electrochemical and thermoelectric metrics, p-HIG SC was selected for detailed thermal charging analysis. Its working mechanism aligned with the HIG thermocapacitor, following four key stages (Fig. 13b):^{12,45} Stage I was the thermal diffusion of Na⁺. Na⁺ migrated directionally under thermal gradients, generating thermovoltage ($S_p \Delta T$, S_p = the ionic Seebeck coefficient for p-HIG). Afterwards, the electric charging stage began, external circuit connection triggers electron transfer, establishing EDLs. Stage III was about thermal equilibrium, the thermal gradient removal induced reverse voltage via ionic redistribution. Finally, stored charges discharge through external loads. Equivalent circuit analysis (Fig. 13c) modelled this process as a conductive pathway powered by $S_p \Delta T$, with simulated charge-discharge curve (the green curve in

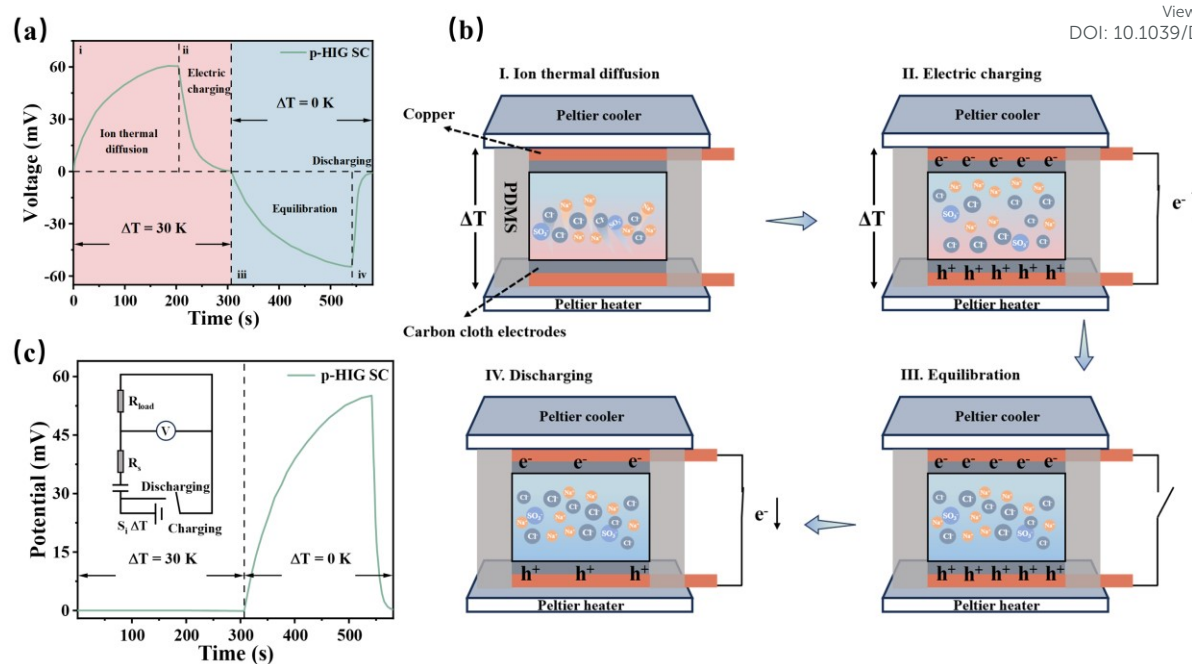


Fig. 13 (a) Thermal voltage curve of HIG SC at different stages under thermal charging state; (b) The working principle diagram of HIG SC; (c) Equivalent circuit diagrams of HIG SC and the charge-discharge curve of capacitor in the equivalent circuit.

Fig. 13c) closely matching experimental data. Especially, p-HIG SC exhibited an initial equilibration period prior to stable thermovoltage generation, corresponding to dynamic balancing between ionic migration and interfacial charge transfer.⁴⁶

As evidenced by the thermal charging curves in **Fig. 13a** and **Fig. S12**, p-HIG SC demonstrated exceptional thermovoltage stability and high ionic thermoelectric efficiency across a broad temperature range (0–40 K). The maximum thermovoltage exhibited progressive enhancement with linearly increasing temperature gradients, maintaining strict linear proportionality ($R^2 > 0.99$). This was a sign of interfacial charge-transfer reliability. The linear response not only validated HIG's operational robustness under variable ambient conditions but also confirmed enhanced ionic thermoelectric efficiency with escalating thermal stimuli. Remarkably, p-HIG SC sustained stable high-voltage output even under extreme thermal loads (40 K ΔT), a breakthrough performance enabling next-generation flexible energy devices for harsh-environment applications.

4. Conclusions

In this work, a high-thermopower ionic thermoelectric hydrogel system for low-grade heat harvesting and intelligent fire protection was prepared by establishing the HIG p-n junctions. The thermoelectric polarity of HIG was reversibly modulated from n-type to p-type through controlled NaCl doping within identical hydrogel matrices. The Seebeck coefficients of n-HIG and p-HIG reached $-1.95 \text{ mV}\cdot\text{K}^{-1}$ and $2.14 \text{ mV}\cdot\text{K}^{-1}$, respectively, while the p-n junction exhibited a much higher Seebeck coefficient of $3.74 \text{ mV}\cdot\text{K}^{-1}$. When being burned, HIG rapidly generated a voltage exceeding 50 mV, and triggered a fire alarm within 4 s, demonstrating excellent thermoelectric efficiency and sensitive early fire-warning capability. Moreover,

HIG exhibited excellent flame retardancy. Even burned on a propane torch for 20 s, HIG could not be ignited. The limiting oxygen index of wood coated with HIG (Wood@HIG) was higher than 90%, and it rapidly self-extinguished after the flame removal. HIG also demonstrated good electrochemical performance and remarkable thermal charging energy storage capabilities, showing great potential for applications in supercapacitors. This work provides new insights for the preparation and application of high fire-safety integrated thermoelectric hydrogel system for energy conversion and storage.

Conflicts of interest

There are no conflicts to declare.

Acknowledgements

We greatly acknowledge the National Natural Science Foundation of China (22478140) and Guangdong Basic and Applied Basic Research Foundation (2023A1515010845, 2024A1515010340) for their financial support.

References

- Z. Li, Y. Xu and X. Zhang, *EnergyChem*, 2024, **6**, 100136.
- W. Yang, J. Bao, H. Liu, J. Zhang and L. Guo, *Renewable Sustainable Energy Rev.*, 2023, **188**, 113842.
- Y. Zhou, Z. Dong, Y. He, W. Zhu, Y. Yuan, H. Zeng, C. Li, S. Chen and K. Sun, *Chemistry – An Asian Journal*, 2022, **17**, e202200850.
- M. Hong and Z. Chen, *Acc. Chem. Res.*, 2022, **55**, 3178–3190.

5. I. López Tobi, M. Comamala, L. Montoro, J. R. González, J. Czarnigowski and A. Gómez, *Energy*, 2024, **313**, 133853.
6. S. Jia, H. Ma, S. Gao, L. Yang and Q. Sun, *Small*, 2024, **20**, 2405019.
7. X. Yang, Z. Zhang, S. A. Khan, L. Sun, Z. Wang, X. Cui, Z. Huang and H. Zhang, *J. Mater. Chem. C*, 2024, **12**, 3298-3305.
8. M. Saleem, F. Ullah, M. T. Qureshi, R. S. Abdel Hameed, M. Abdallah, O. Farghaly, M. Othman and A. Atta, *J. Alloys Compd.*, 2022, **921**, 166175.
9. Y. Yu, X. Xu, M. Bosman, K. Nielsch and J. He, *Nature Reviews Electrical Engineering*, 2024, **1**, 109-123.
10. S. Li, Y. Xu, Z. Li, S. Zhang, H. Dou and X. Zhang, *J. Mater. Chem. A*, 2025, **13**, 3913-3921.
11. H. Cheng and J. Ouyang, *The Journal of Physical Chemistry Letters*, 2022, **13**, 10830-10842.
12. Y. Pai, J. Tang, Y. Zhao and Z. Liang, *Adv. Energy Mater.*, 2023, **13**, 2202507.
13. X. Yang, Y. Tian, B. Wu, W. Jia, C. Hou, Q. Zhang, Y. Li and H. Wang, *Energy Environ. Mater.*, 2022, **5**, 954-961.
14. Z. Lei, W. Gao and P. Wu, *Joule*, 2021, **5**, 2211-2222.
15. Q. Hu, H. Li, X. Chen, Y. Wang, H. Wu, S. Guo and K. Xu, *Adv. Funct. Mater.*, 2024, **34**, 2406968.
16. B. Chen, Q. Chen, S. Xiao, J. Feng, X. Zhang and T. Wang, *Sci. Adv.*, 2023, **9**, eabi7233.
17. N. Chaabene, J. Zhang, M. Turmine, E. Kurchavova, V. Vivier, F. Cuevas, M. Mateos, M. Latroche and J. Monnier, *J. Power Sources*, 2023, **574**, 233176.
18. N. Pereira, L. Afonso, M. Salado, C. R. Tubio, D. M. Correia, C. M. Costa and S. Lanceros-Mendez, *Macromol. Rapid Commun.*, 2024, **45**, 2400041.
19. T. Shimono, M. Matsuki, T. Yamada, M. Morikawa, N. Yasuda, T. Fujigaya and N. Kimizuka, *Chem. Lett.*, 2018, **47**, 261-264.
20. J. Shen, X. Huang, Y. Dai, X. Zhang and F. Xia, *Nat. Commun.*, 2024, **15**, 9305.
21. C. Chi, M. An, X. Qi, Y. Li, R. Zhang, G. Liu, C. Lin, H. Huang, H. Dang, B. Demir, Y. Wang, W. Ma, B. Huang and X. Zhang, *Nat. Commun.*, 2022, **13**, 221.
22. Y. Zhao, Q. Zeng, C. Jiang, X. Lai, H. Li, Z. Wu and X. Zeng, *Nano Energy*, 2023, **116**, 108785.
23. M. Fu, Z. Wu, X. Liu, Y. Yuan, X. Lai and K. Yue, *J. Mater. Chem. A*, 2024, **12**, 27588-27597.
24. W. Qian, S. Jia, P. Yu, K. Li, M. Li, J. Lan, Y. Lin and X. Yang, *Mater. Today Phys.*, 2024, **49**, 101589.
25. A. Shokry, M. M. A. Khalil, H. Ibrahim, M. Soliman and S. Ebrahim, *Sci. Rep.*, 2019, **9**, 16984.
26. J. Ma, F. Zeng, X. Lin, Y. Wang, Y. Ma, X. Jia, J. Zhang, B. Liu, Y. Wang and H. Zhao, *Science*, 2024, **385**, 68-74.
27. Y. Isikver and N. Alkan, *Polym. Bull.*, 2024, **81**, 1019-1042.
28. N. Li, G. Chen, W. Chen, J. Huang, J. Tian, X. Wan, M. He and H. Zhang, *Carbohydr. Polym.*, 2017, **178**, 159-165.
29. C. Li, Y. Zhang, H. Zhao, Z. Yu, J. Zhang, P. Zhang and H. Chen, *J. Mater. Chem. A*, 2024, **12**, 9518-9526.
30. W. Zhao, Y. Zheng, A. Huang, M. Jiang, L. Wang, Q. Zhang and W. Jiang, *Adv. Mater.*, 2024, **36**, 2402386.
31. K. Takada, N. Ohta and Y. Tateyama, *J. Inorg. Organomet. Polym. Mater.*, 2015, **25**, 205-213.
32. J. Li, P. Zhang, H. He and B. Shi, *Mater. Des.*, 2020, **187**, 108373.
33. C. Han, X. Qian, Q. Li, B. Deng, Y. Zhu, Z. Han, W. Zhang, W. Wang, S. Feng, G. Chen and W. Liu, *Science*, 2020, **368**, 1091-1098.
34. Z. Zou, N. Ma, A. Wang, Y. Ran, T. Song, Y. Jiao, J. Liu, H. Zhou, W. Shi, B. He, D. Wang, Y. Li, M. Avdeev and S. Shi, *Adv. Energy Mater.*, 2020, **10**, 2001486.
35. C. Jiang, X. Lai, Z. Wu, H. Li, X. Zeng, Y. Zhao, Q. Zeng, J. Gao and Y. Zhu, *J. Mater. Chem. A*, 2023, **11**, 21368-21378.
36. W. Gan, C. Chen, Z. Wang, J. Song, Y. Kuang, S. He, R. Mi, P. B. Sunderland and L. Hu, *Adv. Funct. Mater.*, 2019, **29**, 1807444.
37. B. Bheemisetty and Lewis SA, *J Appl Pharm Sci*, 2024, **14**, 51-60.
38. Y. Xu, W. Zhang, Y. Qiu, M. Xu, B. Li and L. Liu, *Composites, Part B*, 2022, **238**, 109913.
39. T. Takaoka, R. Nakamura and H. Habu, *Fuel*, 2025, **392**, 134645.
40. W. Yuan, X. Huang, J. Fu, Y. Ma, G. Li and Q. Huang, *Energies*, 2022, **15**, 9055.
41. J. Liu, Z. Yu, H. He, Y. Wang and Y. Zhao, *Cellulose*, 2021, **28**, 8751-8769.
42. L. Liu, J. Feng, Y. Xue, V. Chevali, Y. Zhang, Y. Shi, L. Tang and P. Song, *Adv. Funct. Mater.*, 2023, **33**, 2212124.
43. Q. Zeng, X. Lai, H. Li, Z. Chen, X. Zeng and L. Zhang, *J. Mater. Chem. A*, 2024, **12**, 1642-1653.
44. A. R. Finney and M. Salvalaglio, *Faraday Discuss.*, 2024, **249**, 334-362.
45. D. Kim, Z. A. Akbar, Y. T. Malik, J. Jeon and S. Jang, *Nat. Commun.*, 2023, **14**, 3246.
46. L. Du Hill, M. De Keersmaecker, A. E. Colbert, J. W. Hill, D. Placencia, J. E. Boercker, N. R. Armstrong and E. L. Ratcliff, *Mater. Horiz.*, 2022, **9**, 471-481.

Data available on request from the authors.

[View Article Online](#)
DOI: 10.1039/D5TA04718H

The data that support the findings of this study are available from the corresponding author, Xuejun

Lai, upon reasonable request.